



## Where, when and why? Quantifying the relation of particle deposition to crossflow velocity and permeate water flux in forward osmosis

Anne Bogler<sup>a,\*,1</sup>, Andreas Kastl<sup>b,1</sup>, Markus Spinnler<sup>b</sup>, Thomas Sattelmayer<sup>b</sup>, Avraham Be'er<sup>a</sup>, Edo Bar-Zeev<sup>a,\*</sup>

<sup>a</sup> Zuckerman Institute for Water Research, The Blaustein Institutes for Desert Research, Ben-Gurion University of the Negev, Sde Boqer Campus, Midreshet Ben-Gurion, 8499000, Israel

<sup>b</sup> Lehrstuhl für Thermodynamik, Technische Universität München, Boltzmannstr. 15, 85748, Garching, Germany

### ARTICLE INFO

#### Keywords:

Particle tracking  
Forward osmosis  
Spacer  
Fouling  
Hydrodynamics

### ABSTRACT

Fouling is the main hurdle for all membrane-based systems treating water with high fouling propensity. A novel imaging approach was applied in a forward osmosis (FO) system with spacers to follow *in-situ* and *real-time* deposition of fluorescent beads as bacteria proxy on the membrane using large-field high-resolution epifluorescence microscopy. For the first time, this study quantifies the impact of crossflow velocity (1.3 or 13 cm s<sup>-1</sup>) and permeate water flux (6 or 30 L m<sup>-2</sup> h<sup>-1</sup>) on spatiotemporal patterns of initial cake layer formation (4 h). The total amount of deposited particles on the membrane increased by 84 fold as the ratio of permeate water flux over crossflow velocity,  $D$ , was raised by 54 fold. Spatial distribution of particles was more homogenous at higher  $D$  ratio, while particle accumulation rates decreased by 50% over 4 h. Distribution of local velocities of particle flow paths elucidated the observed spatial deposition patterns. These new quantitative results highlight that the ratio of permeate water flux over crossflow velocity impacts all aspects of particle deposition and may aid in designing new spacer geometries. We also suggest that appropriate hydrodynamic conditions may be a viable tool to postpone the onset of fouling in new and cleaned membrane modules.

### 1. Introduction

Alternative water sources, such as recycled wastewater, are gaining importance due to the growing pressure on natural freshwater sources. A viable avenue for advanced wastewater treatment is forward osmosis (FO), which is driven by an osmotic pressure gradient [1]. Application of FO provides advantages compared to pressure driven membrane systems, including reduced system complexity and lower fouling propensity [2,3]. Microbial fouling (hereafter termed biofouling) is a major challenge in membrane processes, especially for wastewater reclamation [3,4]. Secondary wastewater often contains high concentrations of biodegradable substances and microbes that expedite biofilm formation in membrane modules.

FO technology applies spiral wound modules with high packing density. These modules comprise membrane sheets that are wound around a central tube and are separated by channel spacers, which often

have a net-type geometry [5]. Apart from forming a channel for the feed and draw solutions, spacers also promote turbulence at the membrane surface to minimize the negative effects of concentration polarization [6]. Unfortunately, feed spacers are also linked to the detrimental phenomena of biofilm accumulation and biofouling development [7,8]. However, application of a thicker feed spacer (1.2 mm vs. 0.7 mm) improved FO performance in terms of permeate water flux decline, despite the same biomass accumulation [8]. Although most biofouling studies examine mature biofilm after several days of continuous operation [2,8,9], the initial stage of the formation process may be the most promising starting point for biofouling mitigation.

Biofilm formation commences with the deposition of organic matter and bacterial cells on the membrane [10,11]. Despite the fact that deposited cells may initiate reproduction after few minutes, the foulant cake will develop as a mono-layer until the first biofilm-like microcolonies establish after few hours [10,11]. During this initial stage of

\* Corresponding author.

\*\* Corresponding author.

E-mail addresses: [bogler@post.bgu.ac.il](mailto:bogler@post.bgu.ac.il) (A. Bogler), [kastl@td.mw.tum.de](mailto:kastl@td.mw.tum.de) (A. Kastl), [spinnler@td.mw.tum.de](mailto:spinnler@td.mw.tum.de) (M. Spinnler), [sattelmayer@td.mw.tum.de](mailto:sattelmayer@td.mw.tum.de) (T. Sattelmayer), [beera@bgu.ac.il](mailto:beera@bgu.ac.il) (A. Be'er), [barzeeve@bgu.ac.il](mailto:barzeeve@bgu.ac.il) (E. Bar-Zeev).

<sup>1</sup> These authors contributed equally.

biofilm formation a variety of factors may influence deposition within the membrane channel. Crossflow velocity and permeate water flux are especially important, since both determine the forces that control the path of inert particles or bacterial cells towards the membrane [12,13]. Lift forces generated by crossflow shear carry bacteria away from the membrane surface, hence reducing deposition. Differently, permeate water flux induces a velocity vector component perpendicular to the crossflow and towards the membrane surface, thus enhancing deposition and diminishing re-suspension into the bulk [13,14]. Previous studies have investigated the impact of crossflow and permeate water flux on deposition of particles to determine critical flux or quantify particle detachment by rinsing [13,15]. However, flow conditions in the membrane channel are further influenced by feed spacers and deposition patterns change as distinct spacer configurations and hydrodynamics are applied [16,17]. Impact of spacer configurations and hydrodynamic conditions on deposition were mostly tested in pressure driven systems and compared qualitatively, without quantification of deposited particles, spatial distribution or temporal dynamics. Yet, quantification of deposition in time and space can provide vital information on areas prone to fouling and may lead to new approaches for fouling mitigation.

In this study, the initial deposition (single particles to a monolayer) of fluorescent beads (1  $\mu\text{m}$ ) as bacteria proxy in an FO membrane channel with spacers was investigated quantitatively using new particle detection and tracking approaches. Experiment duration was set to 4 h in order to focus on the initial stages of cake formation. Deposition was captured *in-situ* and *in real-time* and compared between different operating conditions, namely two crossflow velocities (1.3  $\text{cm s}^{-1}$  or 13  $\text{cm s}^{-1}$ ) and two permeate water fluxes (6  $\text{L m}^{-2} \text{h}^{-1}$  or 30  $\text{L m}^{-2} \text{h}^{-1}$ ). Temporal development of particle deposition was examined in 30 s intervals and spatial patterns were analyzed statistically. Flow paths of slowly moving particles close to the membrane surface were captured via particle tracking to elucidate the deposition patterns. The results highlight the importance of applying optimal combinations of crossflow and permeate water flux to minimize foulant deposition.

## 2. Materials and methods

### 2.1. Experimental FO system

A microscope-equipped bench-scale FO system was operated in a closed loop mode for 4 h deposition experiments (Fig. 1A, S1). *In-situ* and *real-time* observation was facilitated by a specially designed 3D printed crossflow cell (Shapeways, USA) that comprised a microscope slide as a viewing window on the feed side (Fig. 1B). Both crossflow cell and experimental system are described in detail in our recent publication [18] and the supporting information.

### 2.2. FO membrane and spacer

A commercial thin-film composite FO membrane (FOMEM-0415, Porifera, USA) was used, with a contact angle of  $\sim 70^\circ$  on the active layer. The membrane area inside the flow cell was  $7.9 \times 3.7 \text{ cm}^2$  and the thickness of the applied spacer (17 mils = 0.43 mm, Conwed®, USA) determined the channel height on feed and draw side. The spacer had a diamond-shaped pattern, comprising two layers of slightly hydrophobic polypropylene filaments (contact angle of  $\sim 94^\circ$ ). Additional information on the FO membrane is provided in the supporting information.

### 2.3. Experimental procedure

After inserting membrane and spacers into the crossflow cell, the system was run overnight with double distilled water (DDW) to remove all air bubbles. The experiment was initiated by adding artificial sterile wastewater stock solution to the feed reservoir (2 L). At the same time, the draw reservoir was supplemented with 5 M NaCl stock solution to reach a total volume of 8 L with the required concentration (up to 1 M) for the desired permeate water flux and draw conductivity was measured (Eutech Instruments, Thermo Scientific, USA, Table S1). A large draw solution volume (8 L) was used to minimize the dilution effect due to cumulative permeate water flux. After 10 to 20 min of stabilization the feed solution was spiked with fluorescent beads (1  $\mu\text{m}$ , FluoSpheres®, Molecular Probes, USA), which are hydrophilic, negatively charged and neutrally buoyant (1.05  $\text{g mL}^{-1}$ ) [19]. Image acquisition was started directly following foulant addition and feed

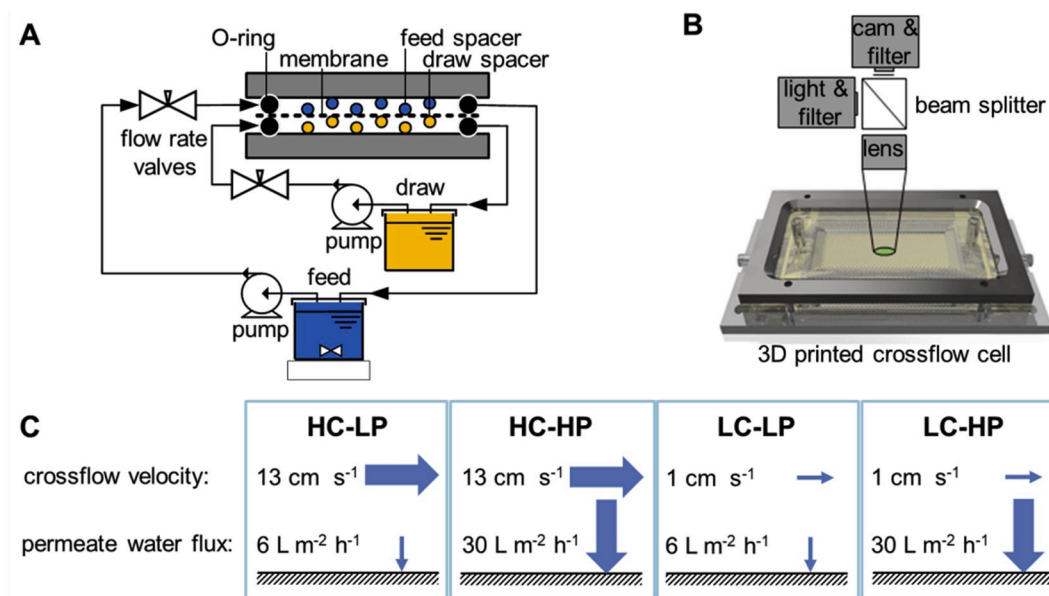


**Fig. 1.** Schematic of the bench-scale FO system comprising the custom-made 3D printed membrane crossflow cell (A). The crossflow cell was equipped with a viewing window and placed under an epifluorescence microscope for continuous observation (B). Summary of the four combinations of high or low crossflow (HC or LC) and high or low permeate water flux (HP or LP) (C).

subsamples were taken every 60 min to measure beads concentration in an Attune NxT flow cytometer (life technologies, Fig. S2). Additional information on experimental procedure, wastewater composition, beads characteristics and concentration as well as flow cytometry can be found in the [supporting information](#).

Four independent sets of experiments were conducted over 4 h with different combinations of permeate water flux and crossflow velocity (Fig. 1C). Crossflow was set to either  $13 \text{ cm s}^{-1}$  (high crossflow, HC) or  $1.3 \text{ cm s}^{-1}$  (low crossflow, LC), while permeate water flux was either  $30 \pm 4.6 \text{ L m}^{-2} \text{ h}^{-1}$  (high permeate water flux, HP) or  $6.4 \pm 0.8 \text{ L m}^{-2} \text{ h}^{-1}$  (low permeate water flux, LP). High crossflow and high permeate water flux (HC-HP) were chosen to mimic the operation of full scale spiral wound FO membrane modules [8,20]. The Reynolds number under this condition was approximately 70, as calculated according to Schock and Miquel 1987 [21] with equation S1 in the [supporting information](#). As a comparison, low crossflow velocity (LC) and low permeate water flux (LP) were reached by lowering crossflow and draw solution concentration, respectively, by one magnitude (Table S1), resulting in a Reynolds number of ca. 7. The tenfold reduction was selected to ensure measurable differences in particle deposition as well as cover a wide range of operating conditions.

## 2.4. Image acquisition

Images were obtained using the software ZEN 2.6 (Zeiss, Germany) to control an epifluorescence microscope (Axio Zoom, V16, Zeiss, Germany) equipped with a PanNeoFluar objective and an Axiocam 506 mono camera. The orange fluorescence of the beads was detected with a Rhodamine filter (ex. 546/12 nm, beam splitter 560 nm, em. 607/80 nm). A spacer element in the middle of the flow cell was chosen for image acquisition in order to eliminate possible effects on deposition from in- and outlet as well as channel walls [16,20]. The area of the spacer element (approx.  $1.5 \times 1.5 \text{ mm}^2$ ) was captured at 20x magnification with the focus on the membrane surface ( $<40 \mu\text{m}$ ). Binning was set at 2 to reduce noise, resulting in images of  $512 \times 512$  pixels with a pixel size of  $4.95 \times 4.95 \mu\text{m}^2$ . Images were taken every 30 s over the experiment duration of 4 h with an exposure time of 100 ms. Additionally, movies of 15 s duration at  $30 \text{ frames s}^{-1}$  with an exposure time of 25 ms were taken at the beginning of the experiments for particle tracking.

## 2.5. Image analysis

For each experiment (three for each condition) the membrane area

within the imaged spacer element was analyzed and the area covered by spacer filaments and beyond was omitted (Fig. 3A). The enclosed membrane area was split into nine regions for further analysis of particle distribution (Fig. 3A). This image analysis procedure for quantification of deposition over time via particle detection and counting, as well as the procedure for particle tracking are described in detail in our previous publication [18]. Briefly, recorded movies were exported from ZEN as sequences of single-frame images and analyzed in MATLAB® (The Mathworks™, Inc.). First, the background was subtracted from each frame and a threshold was applied. In the resulting binary image, patches of interconnected pixels were identified and the number of particles contained in each patch was determined based on the patch's area (5 pixels per particle). For particle tracking, particles were detected in the current frame and assigned to particles in the previous frame via the Euclidian distance between them as well as the movement of the particle in prior frames.

## 2.6. Statistical analysis

The Excel add-in XLSTAT (Addinsoft, USA) was used for statistical analyses. Time series of the number of deposited particles were processed with exponential smoothing to reduce artifacts due to variations in overall intensity between subsequent images. Statistically significant differences were determined at a significance level of  $p < 0.05$  using analysis of variance (ANOVA) and post hoc multiple comparison method of Newman-Keul's (SNK). Correlations were tested with Pearson's correlation test at the same significance level of  $p < 0.05$ .

## 3. Results and discussion

### 3.1. Quantifying the impact of crossflow velocity and permeate water flux on initial deposition of particles

Deposition experiments were conducted over 4 h under four hydrodynamic conditions: high crossflow velocity with high or low permeate water flux (HC-HP; HC-LP) as well as low crossflow velocity with high or low permeate water flux (LC-HP; LC-LP) (Fig. 1C). Deposited particles (DP) were determined as the number of beads that accumulated on the membrane surface over the course of each experiment. Following 4 h of continuous operation, the total number of particles that deposited on the membrane within one spacer element was significantly different between all four hydrodynamic conditions (Figs. 2A and 4A  $t = 4 \text{ h}$ ). The highest number of deposited particles ( $3112 \pm 155 \text{ beads mm}^{-2}$ ) was observed under LC-HP condition, while the lowest number ( $37 \pm 10$

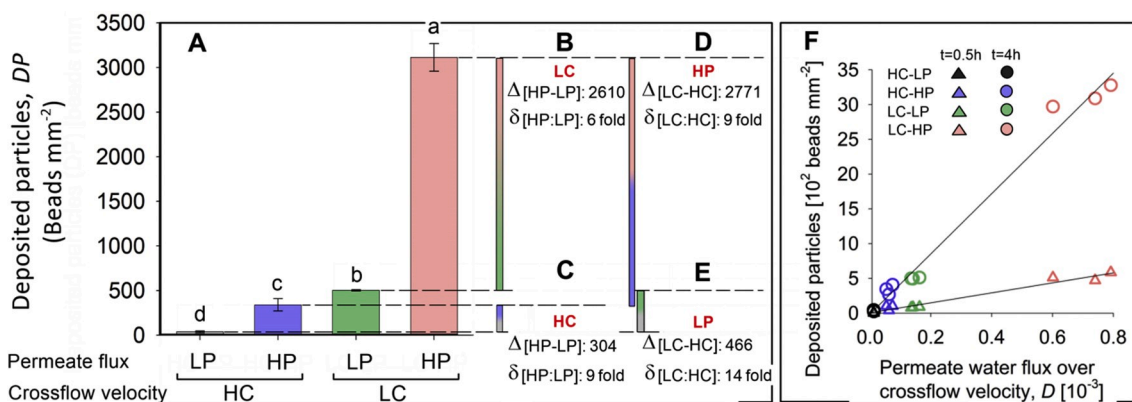


Fig. 2. Total amount of deposited particles (DP) on the membrane surface after 4 h under four hydrodynamic conditions (A): high crossflow (HC) with low or high permeate water flux (LP and HP, respectively), as well as low crossflow (LC) with low or high permeate water flux. ANOVA analysis at a significance level of  $p < 0.05$  resulted in significantly different numbers of deposited particles under all hydrodynamic conditions (a–d). The change in deposited particles as calculated by subtraction ( $\Delta$ ) and division ( $\delta$ ) between high and low permeate water flux was determined under low (B) and high (C) crossflow conditions. Similarly, the same calculations were done for the transition from low to high crossflow velocity under high (D) and low (E) permeate water flux. Deposited particles at different ratios of permeate water flux over crossflow velocity,  $D$ , 0.5 h and 4 h after foulant addition (F).

beads  $\text{mm}^{-2}$ ) was two magnitudes less under HC-LP condition. Although significantly different, the number of particles deposited on the membrane surface under HC-HP ( $349 \pm 69$  beads  $\text{mm}^{-2}$ ) was only slightly lower than under LC-LP condition ( $503 \pm 8$  beads  $\text{mm}^{-2}$ ).

The impact of modifying crossflow velocity and permeate water flux on particle deposition during the initial stage of fouling formation (4 h) was compared using the difference ( $\Delta$ ; HP – LP and LC – HC) and ratio ( $\delta$ ; HP : LP and LC : HC) in deposited particles between hydrodynamic conditions (Fig. 2B – E). The increment in permeate water flux by 5 fold from LP to HP increased deposition by 2610 beads  $\text{mm}^{-2}$  under LC conditions ( $\Delta_{LC} = [DP_{HP} - DP_{LP}]_{LC}$ , Fig. 2B) and by only 304 beads  $\text{mm}^{-2}$  under HC conditions ( $\Delta_{HC} = [DP_{HP} - DP_{LP}]_{HC}$ , Fig. 2C). However, this corresponded to a 6 fold rise in deposition at LC ( $\delta_{LC} = [DP_{HP} : DP_{LP}]_{LC}$ , Fig. 2B), but 9 fold at HC ( $\delta_{HC} = [DP_{HP} : DP_{LP}]_{HC}$ , Fig. 2C). Lowering crossflow velocity from HC to LC by 10 fold raised the amount of deposited particles by 2771 beads  $\text{mm}^{-2}$  under HP conditions ( $\Delta_{HP} = [DP_{LC} - DP_{HC}]_{HP}$ , Fig. 2D), while the increase was 466 beads  $\text{mm}^{-2}$  under LP conditions ( $\Delta_{LP} = [DP_{LC} - DP_{HC}]_{LP}$ , Fig. 2E). Thus, reducing crossflow velocity enhanced the amount of deposited particles by 9 fold under HP conditions ( $\delta_{HP} = [DP_{LC} : DP_{HC}]_{HP}$ , Fig. 2D) and by 14 fold at LP ( $\delta_{LP} = [DP_{LC} : DP_{HC}]_{LP}$ , Fig. 2E). Although higher ratios were obtained for the comparisons comprising HC-LP condition (Fig. 2C and E), the absolute change in the amount of foulant was much higher when hydrodynamic conditions were modified to LC-HP (Fig. 2B and D). Considering that the effect of the foulant layer on concentration polarization and membrane performance is determined by the total amount of foulant on the membrane, changing permeate water flux from LP to HP under LC conditions had the most relevant impact during this initial fouling stage.

Further, the effect of hydrodynamic conditions on deposition was analyzed by the correlation between the number of particles on the membrane surface and the ratio of permeate water flux over crossflow velocity,  $D$  (Fig. 2F). A significant positive correlation was found between deposited particles and  $D$  after 0.5 h of constant operation ( $R^2 = 0.97$ , Pearson's  $r = 0.98$ ,  $p < 0.001$ ) and after every subsequent half hour until 4 h ( $R^2 = 0.99$ , Pearson's  $r = 0.98$ ,  $p < 0.001$ , Fig. 2F). Overall, the amount of deposited particles after 4 h was 84 fold higher under LC-HP than HC-LP condition, while ratio  $D$  was raised by 54 fold. The gap in number of deposited particles between the different ratios  $D$ , namely the four hydrodynamic conditions, increased over time. Consequently, the linear coefficient of the correlation rose from  $7.2 \times 10^5$  beads  $\text{mm}^{-2}$  ( $t = 0.5$  h) to  $43 \times 10^5$  beads  $\text{mm}^{-2}$  ( $t = 4$  h, Fig. 2F). A similar ratio of permeate water flux to crossflow velocity was also defined by Shankararaman and Wiesner 1992, with inclusion of particle size ( $0.05 \mu\text{m}$  to  $10 \mu\text{m}$ , equation S2) [22]. This ratio increases with permeate water flux ( $5 \times 10^{-3}$  to  $6 \times 10^{-2} \text{cm s}^{-1}$ ), but decreases with rising crossflow velocity ( $30$  to  $100 \text{cm s}^{-1}$ ). It was suggested that the drag force of permeate water flux is dominating over the lift force induced by crossflow when that ratio is  $\gg 1$ . Values obtained from the modified ratio were much greater than one for all four hydrodynamic conditions tested here and they were higher by far under LC conditions (Table S2).

These new quantitative comparisons attest to the importance of hydrodynamic conditions regarding the extent of particle deposition. The tested hydrodynamic conditions differed in crossflow velocity and permeate water flux, which are both directly related to the forces that act on particles in the membrane channel. Crossflow promotes shear at the membrane surface, which counteracts deposition via lift forces, while permeate water flux creates a drag force that carries particles towards the membrane surface and enhances deposition [12,16,18,23,24]. Therefore, the ratio between lift and drag forces determines whether particles move towards the membrane surface [22,25], which is a critical factor in the initial stage of fouling formation. This connection was confirmed by the strong correlation between the amount of deposited particles and the ratio of permeate water flux over crossflow velocity,  $D$  (Fig. 2F). Specifically for inert particles, the derived correlation may provide an approximate prediction of particle deposition at other hydrodynamic conditions. On the other hand, lower predictability

according to ratio  $D$  could be expected for bacteria, since the additional factor of growth is relevant and not comprised in the correlation.

Both live and inert particles have previously been observed to follow similar trends than were quantified in this study [13,17,26]. The number of particles that deposit on a surface can be lowered by raising the crossflow velocity, while higher permeate water flux will result in the opposite effect [13,16,17,26]. However, spacers were only included partially in one FO study [26] and deposition was mostly compared qualitatively [16,17]. Deposition of  $3 \mu\text{m}$  latex beads was found to be negligible in FO at a crossflow velocity of  $9 \text{cm s}^{-1}$  up to a critical permeate water flux of  $28 \text{L m}^{-2} \text{h}^{-1}$  [26] or was unaffected by a rise in permeate water flux ( $0$  or  $35 \text{L m}^{-2} \text{h}^{-1}$ ) at a higher crossflow velocity ( $14 \text{cm s}^{-1}$ ) in a pressure-driven system [16]. Smaller particles are less affected by lift forces when compared to particles with a larger diameter [22]. Hence, particle deposition was more likely to occur in our study ( $1 \mu\text{m}$ ) than in the study of Radu et al. [16] ( $3 \mu\text{m}$ ) under similar hydrodynamic conditions. These differences clearly demonstrate the importance and need for exact quantification of deposition for the detailed comparison between operating conditions, foulant concentration and characteristics, including particle size, density, surface properties and type (*i.e.* live/inert).

In addition to transport of particles from the bulk to the liquid-membrane interface, particle deposition comprises a second phase, namely the attachment (reversible and irreversible) to the membrane surface. Attachment relies mainly on interfacial forces between particles and membrane surface, including long-range interactions of electrostatic repulsion. Electrostatic repulsion of charged particles, such as the negatively charged beads used here, decreases with higher feed solution ionic strength and can thus enhance attachment [14,25]. Calculation of reverse solute flux (Table S3) indicated a rise in bulk feed concentration by up to 10% after 4 h operation at HP, which is insufficient to significantly impact electrostatic repulsion [25]. However, since ionic strength at the membrane surface is determined by concentration polarization, which depends on mass transfer in the channel, hydrodynamic conditions also impact this aspect of particle deposition [16,22,26]. Ionic strength at the feed membrane surface was estimated to be similar at both HC conditions due to strong mixing (Table S3) [27]. Yet, higher reverse salt flux caused nearly 5 fold higher ionic strength at the membrane surface under LC-HP condition than under LC-LP, which could have diminished electrostatic repulsion [25]. Therefore, it is possible that the deposition at LC-HP condition was not only enhanced by the high ratio of permeate water flux over crossflow velocity, but was further expedited by lower electrostatic repulsion. Insights into the mechanisms that influence initial deposition might have severe implications when considering spacer filled channels, since permeate water flux and crossflow velocity vary in space and time.

### 3.2. Where? Resolving the spatial patterns of particle deposition within a spacer element

The spatial deposition patterns that developed under the four hydrodynamic conditions were quantified by dividing the area within the spacer element into nine regions, defined according to cardinal directions (Fig. 3A). The crossflow was directed from West to East and spacer filaments I and III (South-West and North-East direction) were in contact with the glass, while filaments II and IV (North-West and South-East direction) were in contact with the membrane surface (Fig. 3B and C).

Each combination of crossflow velocity and permeate water flux resulted in a significantly different spatial distribution pattern of deposited particles after 4 h of constant operation (Fig. 3D – K). Under HC-LP condition, only a narrow area upstream of spacer filament III contained deposited particles (Fig. 3D). The area containing particles expanded as permeate water flux was increased to HC-HP condition. Hence, the deposition front, namely the border between the covered and free area, shifted to the middle of the spacer element (dashed line,

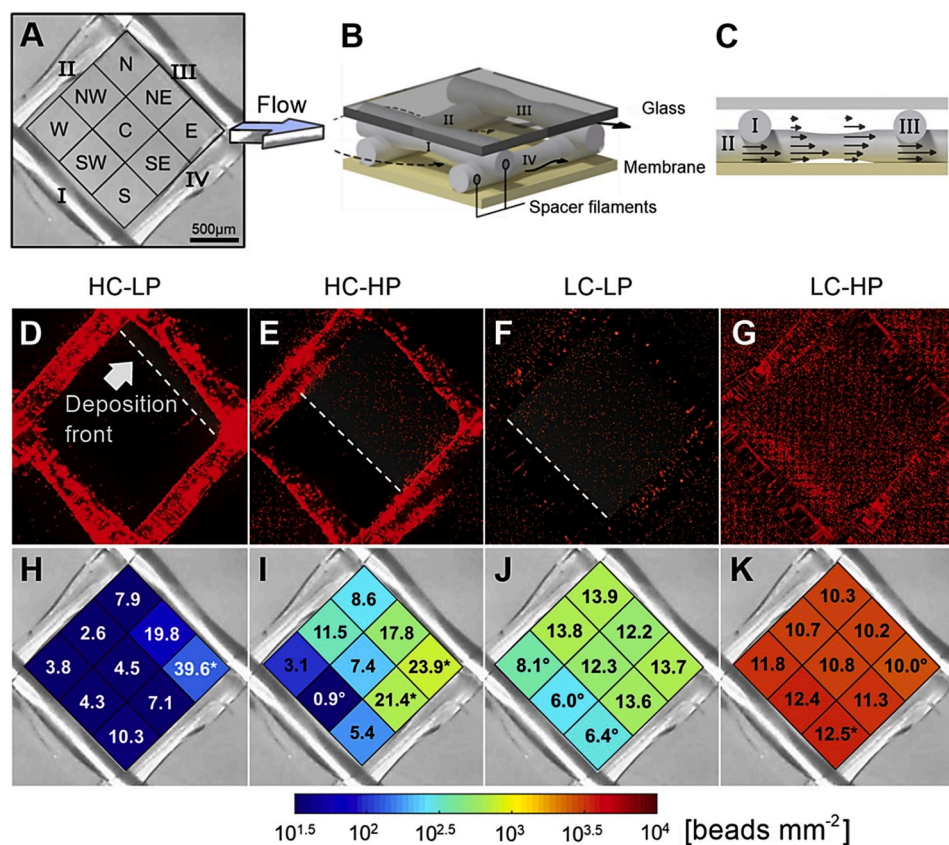


Fig. 3E). The deposition front crossed the middle of the spacer element at LC-LP, leaving only a narrow area with few deposited particles downstream of filament I (*i.e.* between the filament and the deposition front, Fig. 3F). Finally, the whole membrane area within the spacer element was covered by deposited particles under LC-HP condition (Fig. 3G).

It is likely, that the deposition front indicates which areal percentage of the spacer element was affected by the rise in shear rates due to spacer filament I [28]. Local flow velocities were previously shown to increase due to a reduction in channel height, leading to higher shear rates [23, 29,30], created here by the constricted space between filament I and the membrane surface. Under HC-LP condition, the acceleration of flow due to filament I reached the next filament III and minimized deposition within nearly the whole area of the spacer element (> 85%). Contrarily, the higher permeate water flux redirected the flow towards the membrane surface at HC-HP, enhanced drag forces and lowered flow velocity sufficiently for deposition to occur up to more than the middle of the spacer element (32%). The reduction in crossflow at LC-LP further diminished the area of accelerated flow (10%) and moved the deposition front closer to filament I. Finally at LC-HP, deposition commenced directly downstream of this filament, since the flow acceleration due to the restriction in channel height was insufficient to prevent deposition at any area within the spacer element.

Concurrently to the location of the deposition front, the number of particles deposited in the dissected regions was expressed in percent of the total number of particles within the spacer element and compared using statistical analysis (ANOVA,  $p < 0.05$ , Fig. 3H – K). Quantification of the deposited particles separated between the nine regions allowed derivation of the “homogeneity” of the spatial distribution. Homogeneity was calculated as the ratio between the percentage of the regions with the highest and lowest amount of deposited particles. Values of homogeneity close to 1 can be considered as homogeneous, while values above 10 will be referred to as heterogeneous. Thus, spatial distribution was homogeneous under LC-HP condition with a ratio of 1.25 between

the two regions with the highest (South) and lowest (East) amount of deposited particles. However, the amount of deposited particles was still significantly higher in the South (12.5%) and lower in the East (10%) as compared to the other regions. Contrastingly, the East had the highest accumulation under both HC conditions and the distribution was heterogeneous with ratios of 28 at HC-HP and 19 at HC-LP. The highest accumulation in the East (24%) spread into the adjacent Southeast and Northeast regions under HC-HP condition, where the Southwest held less than 1% of the total deposition. Similarly, under LC-LP condition the Southwest (6%) also had the lowest deposition, followed by the South and West regions, but the distribution was more homogenous (2.2).

Spatial deposition patterns as quantified above have only been described qualitatively for comparison of different spacer configurations [16,17]. A clear edge of deposition, namely a sharp transition between areas with and without deposited particles, was previously observed in experiments with the same spacer orientation of a 45° angle between filaments and crossflow direction [17]. However, the edge was oriented in the opposite direction: parallel to spacer filaments II and IV, which are in contact with the membrane, instead of filaments I and III (Fig. 3A) [17]. Under similar operating conditions as HC-HP, distinctive patches with deposited particles were previously observed, that coincide partially with areas of high deposition quantified here (Fig. 3E and I) [16]. It was suggested that deposition upstream of filament crossings was caused by sudden changes in flow direction and velocity reduction due to the complete obstruction of the channel [16,28], which corresponds to the high deposition in East and Southeast regions (Fig. 3E and I). Further deposition patches correlated with sections of thinner filament diameter [16]. However, this effect only caused a small accumulation of particles very close to filament II in the Northeast region (Fig. 3E), since the spacer used in this study had nearly straight filaments.

Taken all of the above, this study quantitatively determined for the first time, how the ratio between permeate water flux and crossflow

velocity affects spatial deposition patterns (Fig. 3D – K). Additionally, differences between these results and previous studies [16,17,25] highlight that spacer geometry as well as particle size and density affect spatial distribution of deposition. These factors determine which of the forces (*i.e.* drag or lift) are relevant at which location under a specific combination of crossflow velocity and permeate water flux. Thus, crossflow velocity and permeate water flux are decisive for the homogeneity of particle deposition in space and if local disturbances created by the spacer filaments concentrate particles in specific areas. Therefore, spacer modifications need to be tested at a range of hydrodynamic conditions to determine their effectiveness across the whole membrane module.

### 3.3. When? Specifying the dynamic development in particle deposition under different hydrodynamic conditions

The membrane surface within a spacer element was imaged every 30 s during 4 h, allowing dynamic quantification of particle deposition. The cumulative deposition is given by the number of particles detected on the membrane surface at each time point. Initial particle deposition commenced immediately upon the addition of beads into the feed solution under all hydrodynamic conditions and continued steadily (Fig. 4A). After only 30 min of FO operation the amount of deposited particles at LC-HP was significantly higher (> 4 fold) than at the other hydrodynamic conditions. After 1 h the number of deposited particles at HC-LP was much lower (> 18 fold) than the other conditions, followed by complete differentiation between all four hydrodynamic conditions after 2 h (Fig. 4A). Total deposition over time developed with a linear positive trend under all hydrodynamic conditions ( $R^2 > 0.92$ , Pearson's  $r > 0.992$ ,  $p < 0.001$ , Fig. 4A).

Concurrently, the particle accumulation rate, defined here as the change in number of particles on the membrane over one time interval, was determined during the initial stage of fouling formation (Fig. 4B). Specifically, the accumulation rate resulted from the sum of particles depositing and detaching from the membrane surface within one spacer element. A “negative accumulation rate” is defined, when more particles were detached than deposited in one time interval. Our results indicated that accumulation rates decreased significantly (50%) from the first to the fourth hour under all conditions, except HC-LP (Fig. 4B). Contrarily, the accumulation rate nearly doubled over the duration of the experiments under HC-LP condition.

Steady flow conditions and constant concentration of particulate foulants in the feed solution (Fig. S3) led to a linear trend of cumulative deposition over time. The slope, namely the average accumulation rate, was significantly different between hydrodynamic conditions during all 4 h. Specifically, the extreme accumulation rate in the first hour under LC-HP condition ( $13 \pm 5.0$  beads  $\text{mm}^{-2} \text{min}^{-1}$ , 81 fold higher than HC-LP) led to significantly higher numbers of deposited particles after only 30

min. Accumulation rates under HC-HP ( $1.5 \pm 1.46$  beads  $\text{mm}^{-2} \text{min}^{-1}$ ) and LC-LP ( $2.2 \pm 1.30$  beads  $\text{mm}^{-2} \text{min}^{-1}$ ) conditions were similar (10 and 13 fold higher than HC-LP, respectively), thus the two conditions required more time (2 h) to become significantly different in the number of deposited particles. Time intervals with negative accumulation rates (*i.e.* detachment events) occurred under all hydrodynamic conditions, except for LC-HP. Deposited particles were therefore less likely to detach again under this condition as compared to HC-LP, where ~20% of time intervals showed negative accumulation rates. It is surmised here that higher permeation drag as well as lower electrostatic repulsion, due to stronger concentration polarization [12], hindered particle detachment from the membrane and re-suspension to the bulk under LC-HP condition, while more particles were reversibly attached under HC-LP condition.

Accumulation rates varied significantly from the first to the last hour under all hydrodynamic conditions. The decrease in accumulation rate may be due to the fact that fouling layers generally acquire a steady state after a certain time of constant operation [14]. Steady state of a fouling layer is defined as the condition in which the forces moving particles towards and away from the membrane are in equilibrium. Therefore, the same amount of foulant is deposited and removed during each time interval, such that the total amount on the membrane remains constant. Although steady state was not yet reached in our experiments, a continued decline in accumulation rate could be expected until the total amount of deposited particles reaches a plateau, the value of which is determined by hydrodynamic conditions and physical properties. As fouling progresses, permeation drag lessens due to cake enhanced concentration polarization until it is in balance with crossflow lift forces. Although this mechanism can contribute to reaching the steady state, it was unlikely relevant here, since the foulant cake was a monolayer of beads with very little impact on concentration polarization [17].

However, the foulant cake may contribute a different mechanism, since already deposited particles can influence the probability of deposition for subsequent particles. On the one hand, shear-induced diffusion due to particle-particle interactions can reduce the probability of approaching particles to deposit [14,31]. Thus, accumulation rates declined as more particles were already accumulated on the membrane surface. On the other hand, single deposited particles can alter local flow conditions and cause approaching particles to deposit [14]. This mechanism may be especially relevant in the first moments of fouling and during operation at HC-LP condition, where only low numbers of particles have yet deposited. We suggest that the higher accumulation rate measured at the end of HC-LP experiments could have been the result of an augmented number of particles on the membrane affecting the local flow field around them, while particle-particle repulsion was not yet influential due to the low surface coverage. Over longer time (> 4 h), it is likely that the amount of particles on the membrane would rise to a level where shear-induced diffusion will become relevant also at

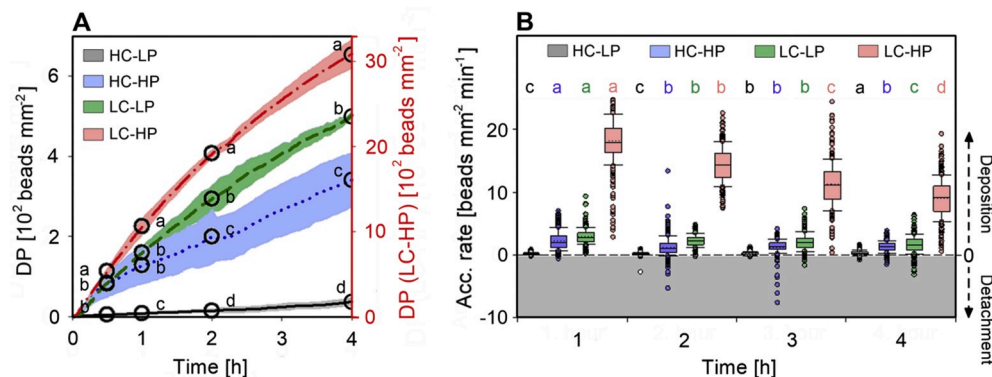


**Fig. 4.** Amount of deposited particles (DP) over time (A) and accumulation rates (B) at the four hydrodynamic conditions: high crossflow with low permeate water flux (HC-LP), high crossflow with high permeate water flux (HC-HP), low crossflow with low permeate water flux (LC-LP) and low crossflow with high permeate water flux (LC-HP). DP at LC-HP is shown on the right y-axis as indicated by the red color (A). Small letters (a–d) indicate statistically significant differences obtained via ANOVA analysis with  $p < 0.05$ : between hydrodynamic conditions at one point in time (A) or between hours under the same hydrodynamic condition (B). (For interpretation of the references to color in this figure legend, the reader is referred to the Web version of this article.)

HC-LP condition, thus leading to a subsequent decrease in accumulation rate that did not yet occur here.

Additionally to the above analysis of accumulation rates within the whole spacer element, cumulative deposition was also determined separately for each region, as shown for those with the highest and lowest deposition as well as the center (C) of the spacer element (Fig. 5). The center was most similar to the region with the lowest deposition under HC conditions (Fig. 5A and B), while it was nearly the same as the one with the highest deposition under LC-LP condition (North, Fig. 5C) and in between the regions of highest and lowest deposition under LC-HP (Fig. 5D). According to the standard deviations from the averages (shaded areas in Fig. 5), the amount of particles within a region was more variable at HC than at LC conditions. Variability was especially high in regions with the highest amount of deposited particles under each hydrodynamic condition (e.g. East at HC, Fig. 5A and B). Contrarily, the final spatial distribution between regions in one spacer element observed after 4 h, was already established after ca. 2 h in HC experiments, and took ca. 3 h to manifest at LC conditions.

Both the distinct heterogeneity in the amount of deposited particles between regions (Figs. 3 and 5) as well as the different time points for establishment of final distribution patterns can be explained by analysis of regional accumulation rates. The pronounced heterogeneity resulted from a greater range of accumulation rates under HC conditions. The range was greatest under HC-LP with the lowest accumulation rate of  $0.005 \text{ beads mm}^{-2} \text{ min}^{-1}$  in the Northwest region and the highest rate of  $0.804 \text{ beads mm}^{-2} \text{ min}^{-1}$  in the East (160 fold more). Concomitantly, the smallest range was observed under LC-HP with accumulation rates ranging from  $6 \text{ beads mm}^{-2} \text{ min}^{-1}$  to  $18 \text{ beads mm}^{-2} \text{ min}^{-1}$  (3 fold). The greater difference in accumulation rates and accordingly in the number of deposited particles between regions (Fig. 5) also accelerated the establishment of the significant differences between regions at HC, compared to the similar accumulation rates at LC. This detailed analysis

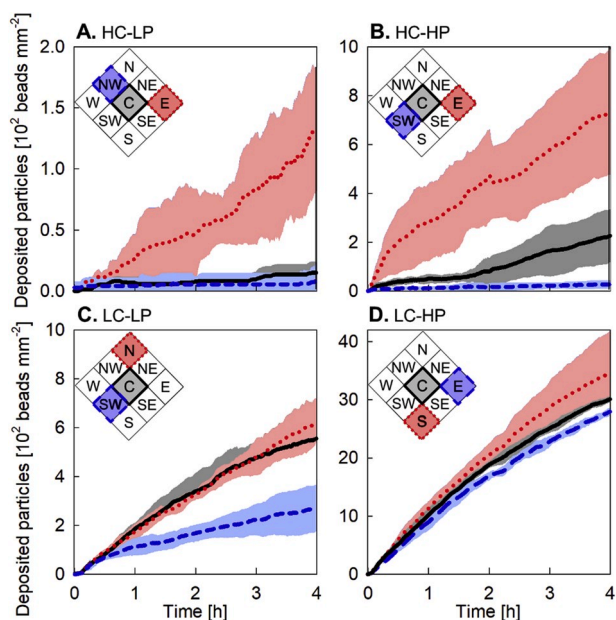


**Fig. 5.** Deposition of beads over time in the region with the highest (red) and lowest (blue) deposition as well as the center region (C, black). Deposition of beads was analyzed at the four hydrodynamic conditions: high crossflow with low permeate water flux (HC-LP, A), high crossflow with high permeate water flux (HC-HP, B), low crossflow with low permeate water flux (LC-LP, C) and low crossflow with high permeate water flux (LC-HP, D). Note the different scaling of the y-axes. Deposition was quantified at 30 s intervals and is shown as the average of three experiments with the shaded area representing one standard deviation. (For interpretation of the references to color in this figure legend, the reader is referred to the Web version of this article.)

of accumulation rates over time within the whole spacer element as well as in the separate regions shows that development of the foulant cake is both dependent on time and hydrodynamic conditions. Such insights may help in determining the required duration of mitigation studies and the optimal time point for initiation of cleaning procedures in operational FO membrane systems.

#### 3.4. Why? Elucidating the effects of crossflow velocity and permeate water flux on particle flow paths close to the membrane surface

In this study, spacer filaments formed a  $45^\circ$  angle with the overall crossflow direction (left to right, Fig. 6). Beads were captured for particle tracking between the membrane surface and up to  $40 \mu\text{m}$  into the bulk. Flow fields were calculated from at least 120 particle tracks for each hydrodynamic condition. It is surmised here that the flow fields obtained from particle tracks represent the flow of the fluid parallel to the membrane surface, since neutrally buoyant particles ( $1.05 \text{ g mL}^{-1}$ ) are assumed to follow the fluid flow [22]. Average velocity of all particle tracks decreased in the order: HC-LP ( $1941 \mu\text{m s}^{-1}$ ) > HC-HP ( $1021 \mu\text{m s}^{-1}$ ) > LC-LP ( $619 \mu\text{m s}^{-1}$ ) > LC-HP ( $410 \mu\text{m s}^{-1}$ ). The maximum particle velocity was approximately twice higher than the average velocity at LP conditions, while it was three times higher at HP conditions (Fig. 6).

Differences in average velocity between experiments with the same crossflow velocity but different permeate water flux indicated that the latter incurred a significant change in particle velocities close to the membrane surface. Higher permeate water flux increases particle concentration at the membrane surface, where crossflow velocities are lowered due to the laminar velocity profile [24,25,32]. When more particles are moving at a lower velocity, the average is reduced compared to the maximum velocity. This effect was apparent from the higher ratio between maximum and average velocity at HP versus LP conditions. Lower particle velocities ( $17 \mu\text{m s}^{-1}$ ) closer to the membrane surface ( $0 - 7 \mu\text{m}$ , Fig. S4) were further confirmed when particle tracks were obtained at higher magnification (60x) [18]. On the other hand,

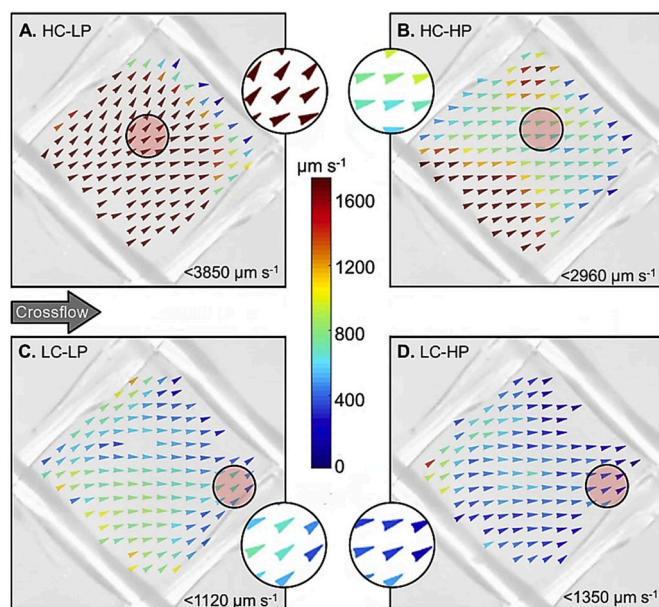


**Fig. 6.** Particle flow paths obtained at the four hydrodynamic conditions: high crossflow with low permeate water flux (HC-LP, A), high crossflow with high permeate water flux (HC-HP, B), low crossflow with low permeate water flux (LC-LP, C) and low crossflow with high permeate water flux (LC-HP, D). Arrows indicate the flow direction, while the color scale represents the flow velocity. Flow paths were calculated from at least 120 particle tracks for each condition. (For interpretation of the references to color in this figure legend, the reader is referred to the Web version of this article.)

particle velocities were measured at greater distances from the membrane surface in similar particle imaging velocimetry studies (30 – 70  $\mu\text{m}$ ) [20,28,33] compared to this study (0 – 40  $\mu\text{m}$ ). This difference may explain the higher velocities (few  $\text{cm s}^{-1}$ ) as compared to the study presented here (few  $\text{mm s}^{-1}$ ). However, it is likely that the absence of permeate water flux was an additional reason for higher particle velocities [20,28]. These results highlight that permeate water flux must be accounted for in particle deposition studies using membrane-based systems, even though it is magnitudes lower than operational crossflow velocities [16,17,23,32].

Higher velocities parallel to the membrane surface can decrease deposition by augmenting the shear rate at the membrane surface [12]. In the obtained results, average velocity was inverse to the total amount of deposited particles (Fig. 2A), confirming that the effect of velocity on the shear rate was decisive for deposition. The highest amount of deposited particles (LC-HP) was 84 fold higher than the lowest (HC-LP), while the average velocity rose by 6 fold from LC-HP to HC-LP. Therefore, particle velocity parallel to the membrane surface had an additional effect on total particle deposition in combination with the ratio of permeate water flux over crossflow velocity, which was 54 fold higher.

Furthermore, accordance between the spatial distribution of the flow velocity (Fig. 6) and the spatial deposition patterns (Fig. 3) provides an additional indication on the effect of flow velocity and shear on particle deposition. Under HC-LP condition, reduction in particle velocities close to filament III and along filament IV (Fig. 6A) lead to particle deposition in Northeast and East regions (Fig. 3H). At HC-HP condition velocities were highest close to filament I (particle entrance into the spacer element, Fig. 6B), resulting in minimal deposition in these regions (Fig. 3I). Additionally, the local increase in particle velocity in the North was likely the cause for the lower deposition compared to the adjacent regions. Most particles were slower ( $< 800 \mu\text{m s}^{-1}$ ) under LC conditions than at HC ( $< 2400 \mu\text{m s}^{-1}$ ). Accordingly, velocity field and spatial distribution of particle deposition were more homogenous (Fig. 6C and D, 3J and K). At LC-LP, high particle velocities close to filament I (Fig. 6C) agree well with lower deposition in the West, Southwest and South regions (Fig. 3J). Most discrepancies between distribution of velocity and deposition were found under LC-HP condition. Although the lowest velocities were observed along filament III (Fig. 6D), these regions accounted for the least deposition (Fig. 3K). Yet, higher local velocities in the West and center corresponded to lower deposition as compared to adjacent regions.

Distribution of deposited particles between regions may further be influenced by the local flow direction, which determines if more particles are transported into or out of a region. Generally, particles entered the spacer element by passing under filament I in a perpendicular direction and left the spacer underneath filament III. Under HC-LP condition, the flow field diverged (Fig. 6A), which was also observed in previous studies at similar crossflow velocities (0.10  $\text{m s}^{-1}$  and 0.16  $\text{m s}^{-1}$ ) [20,28,33]. In contrast, under HC-HP condition the flow field was very uniform (Fig. 6B). All particle paths showed gradual alignment with the overall flow direction. Only some particles were found to enter the spacer element underneath filament II in contact with the membrane, which indicates a gap between filament and membrane. We surmise that the higher permeate water flux led some particles toward the membrane surface, that then passed underneath the spacer filament. Under LC-LP condition, only particles moving in close proximity ( $< 300 \mu\text{m}$ ) to the spacer filaments II and IV continued in the same direction after entering the element, namely parallel to these filaments (Fig. 6C). In the rest of the enclosed area, particles were oriented in the overall crossflow direction (West to East). Especially close to filament IV ( $< 210 \mu\text{m}$ ), the tendency of particles to flow parallel to filaments was further reduced when permeate water flux was raised from LC-LP to LC-HP (see magnification in Fig. 6C and D).

Following the detailed description above, particles moved mainly parallel to the spacer filaments at HC conditions, while the majority was aligned with the overall crossflow direction at LC conditions. The

growing influence of the overall crossflow direction on local flow direction with decreasing crossflow velocity has previously been observed in pressure driven membrane systems [33]. Due to this alignment with the overall crossflow direction under LC conditions, a tendency for particles to be transported away from filament II and towards filament IV could be expected. However, higher deposition in the South, Southeast and East regions as compared to the West, Northwest and North occurred under HC conditions, where the flow paths were less aligned (Figs. 3 and 6). We surmise that high permeate water flux (30  $\text{L m}^2 \text{h}^{-1}$ ) has a decisive impact on the deposition when cross flow is low (1.3  $\text{cm s}^{-1}$ ) with minimal compatibility to the flow paths during these initial stages of cake formation. Accordingly, the spatial distribution of particles within a spacer element is mainly the result of particle velocity and not local flow directions.

#### 4. Conclusions and implications for fouling mitigation

This study provides the first detailed quantitative analyses of the effects imposed by crossflow velocity and permeate water flux on the spatiotemporal patterns of particle deposition during the initial stage of fouling formation in a spacer filled FO channel. The ratio of permeate water flux over crossflow velocity,  $D$ , was increased by 54 fold between the investigated hydrodynamic conditions (Fig. 7) and directly impacted particle deposition as a driving variable via permeation drag and lift forces. Significant differences were quantified between hydrodynamic conditions in terms of total particle deposition, spatial distribution, accumulation rates and particle flow paths.

The total number of deposited particles within a spacer element rose up to 84 fold when the driving variable of ratio  $D$  was augmented (Fig. 7). Changing hydrodynamic conditions was also estimated to raise salt concentration at the membrane surface by approximately 5 fold (Fig. 7), which may have enhanced deposition further via reduced electrostatic repulsion. Additionally, dissection of the spacer element into regions allowed assessment of where particles deposited: High crossflow conditions concentrated most particles upstream of filament crossings ( $> 15$  fold), while the distribution was homogenous under low crossflow conditions ( $< 3$  fold, Fig. 7). When particles deposited, was unraveled by imaging at 30 s intervals. A 50% decline in accumulation rates was computed, except for a 100% increase under high crossflow velocity with low permeate water flux (Fig. 7). Overall, lower crossflow velocity and higher permeate water flux diminished particle velocities at the membrane surface by nearly 5 fold (Fig. 7), thus increasing probability of attachment. The reduction in local flow velocities explained why particles accumulated in the East region at high crossflow velocities, in contrast to the homogenous distribution at low crossflow velocities.

This study provided the first quantitative description on how crossflow velocity and permeate water flux impact spatiotemporal patterns in the initial stage of fouling formation, which are critical for newly installed and freshly cleaned membrane modules. As few hours are required for live bacteria to establish irreversible attachment to the membrane surface, the focus on the initial stage of fouling layer formation may also allow extrapolation of our results to biofilm formation and biofouling development. Moreover, investigation of deposition of additional particle types, sizes, densities and surface characteristics on other surfaces including commercial or modified membranes and spacers could generalize the obtained insights to a wider range of foulants and operating conditions. The complex composition of wastewater also warrants investigation of particle deposition in the presence of compounds, which may cause additional fouling mechanisms (e.g., scaling and organic fouling) or various chemical interactions with the particles.

Our results showed, that optimization of hydrodynamic conditions may be a viable approach to postpone fouling onset. However, improved system efficiency needs to outweigh the additional pumping costs or membrane area that are required at higher crossflow velocities and

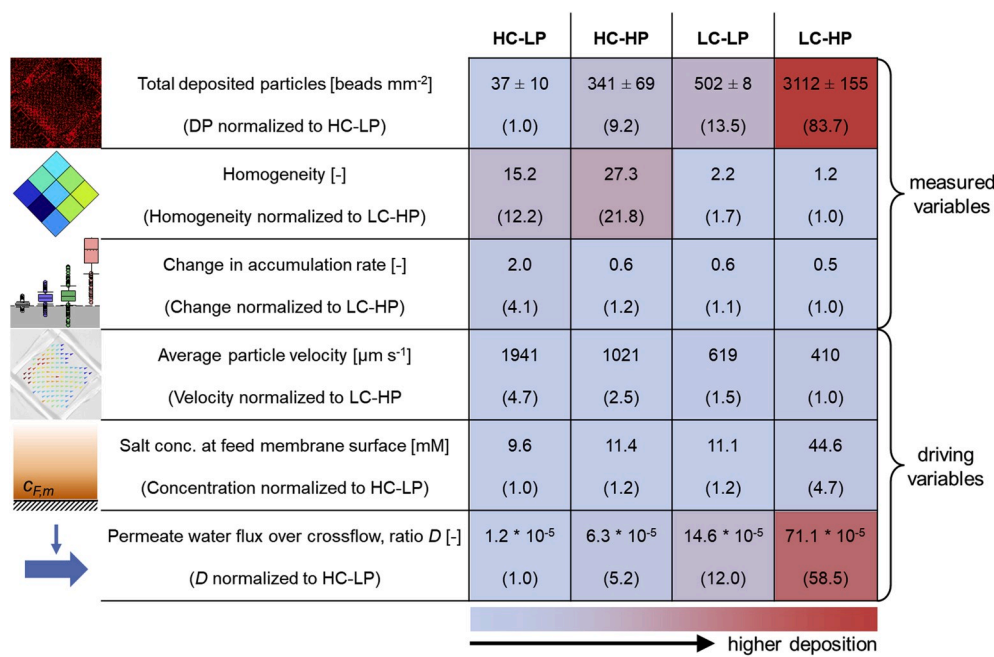


**Fig. 7.** Quantitative and visualized comparison of measured variables (total deposited particles, homogeneity, accumulation rate) and driving variables (average particle velocity, feed membrane concentration and ratio of permeate water flux over crossflow velocity, *D*) at four hydrodynamic conditions: high crossflow with low permeate water flux (HC-LP), high crossflow with high permeate water flux (HC-HP), low crossflow with low permeate water flux (LC-LP) and low crossflow with high permeate water flux (LC-HP). Variables were normalized to the condition with the smallest value and normalized values are given in parentheses for better comparison. The color scale visualizes the effect of the variables on deposition with red for high deposition/high positive impact on deposition. (For interpretation of the references to color in this figure legend, the reader is referred to the Web version of this article.)

lower permeate water flux, respectively. Further, it is important to note that crossflow velocity and permeate water flux vary over the length of an operational spiral wound module due to the concentration of feed water and dilution of the draw solution. We stress that fouling mitigation approaches should be tested to ensure effectiveness under a range of hydrodynamic operating conditions, and with different particle types (live/inert) and sizes (nano-micro scale). Detailed spatial analysis developed in this study can provide starting points for the development of modified spacer geometries for fouling mitigation, while temporal patterns can indicate the optimal time point for initiation of cleaning procedures.

#### Author contributions

The manuscript was written through contributions of all authors. All authors have given approval to the final version of the manuscript.

#### Declaration of competing interest

The authors declare that they have no competing financial interests or personal relationships that could have appeared to influence the work reported in this paper. There is no conflict of interest and all co-authors have seen and approved the current version for submission.

#### Acknowledgment

The authors gratefully acknowledge Porifera, USA, and James Kidwell from Conwed Plastics LLC, USA, for providing FO membrane samples and spacer samples, respectively. We thank the Kreitman School for Advanced Graduate studies and the Zuckerberg Institute of Water Research of Ben-Gurion University of the Negev, Israel, for granting the “Negev Tsin Scholarship” and the “ZIWR Excellence scholarship”, respectively, to Anne Bogler, as well as the Rieger Foundation and the Jewish National Fund for their support through Anne’s Rieger Foundation-Jewish National Fund Fellowship in Environmental Studies in the 2018–2019 schoolyear. We also acknowledge the support by the BMBF-MOST Young Scientist Exchange program, YSEP133, awarded to Andreas Kastl. Avraham Be’er thanks the Israel Science Foundation Grant No. 373/16 for partial support. Edo Bar-Zeev thanks the Roy J Zuckerberg Career Development foundation. This paper is in partial

fulfillment of the Ph.D. thesis by Anne Bogler at Ben-Gurion University of the Negev.

#### Appendix A. Supplementary data

Supplementary data to this article can be found online at <https://doi.org/10.1016/j.memsci.2020.118055>.

#### References

- [1] B.D. Coday, P. Xu, E.G. Beaudry, J. Herron, K. Lampi, N.T. Hancock, T.Y. Cath, The sweet spot of forward osmosis: treatment of produced water, drilling wastewater, and other complex and difficult liquid streams, *Desalination* 333 (2014) 23–35.
- [2] H. Yoon, Y. Baek, J. Yu, J. Yoon, Biofouling occurrence process and its control in the forward osmosis, *Desalination* 325 (2013) 30–36.
- [3] S.E. Kwan, E. Bar-Zeev, M. Elimelech, Biofouling in forward osmosis and reverse osmosis: measurements and mechanisms, *J. Membr. Sci.* 493 (2015) 703–708.
- [4] W. Guo, H.-H. Ngo, J. Li, A mini-review on membrane fouling, *Bioresour. Technol.* 122 (2012) 27–34.
- [5] J.E. Kim, S. Phuntsho, F. Lotfi, H.K. Shon, Investigation of pilot-scale 8040 FO membrane module under different operating conditions for brackish water desalination, *Desalin. Water Treat.* 53 (2014) 2782–2791.
- [6] G.A. Fimbres-Weihs, D.E. Wiley, Numerical study of mass transfer in three-dimensional spacer-filled narrow channels with steady flow, *J. Membr. Sci.* 306 (2007) 228–243.
- [7] J.S. Vrouwenvelder, D.A. Graf von der Schulenburg, J.C. Kruithof, M.L. Johns, M.C. M. van Loosdrecht, Biofouling of spiral-wound nanofiltration and reverse osmosis membranes: a feed spacer problem, *Water Res.* 43 (2009) 583–594.
- [8] R. Valladares Linares, S.S. Bucs, Z. Li, M. AbuGhdeeb, G. Amy, J.S. Vrouwenvelder, Impact of spacer thickness on biofouling in forward osmosis, *Water Res.* 57 (2014) 223–233.
- [9] S.E. Kwan, E. Bar-Zeev, M. Elimelech, Biofouling in forward osmosis and reverse osmosis: measurements and mechanisms, *J. Membr. Sci.* 493 (2015) 703–708.
- [10] H.-C. Flemming, G. Schaule, T. Griebe, J. Schmitt, A. Tamachkiorowa, Biofouling - the Achilles heel of membrane processes, *Desalination* 113 (1997) 215–225.
- [11] E. Bar-Zeev, I. Berman-Frank, O. Girshevitz, T. Berman, Revised paradigm of aquatic biofilm formation facilitated by microgel transparent copolymer particles, *Proc. Natl. Acad. Sci. U.S.A.* 109 (2012) 9119–9124.
- [12] A. Bogler, S. Lin, E. Bar-Zeev, Biofouling of membrane distillation, forward osmosis and pressure retarded osmosis: principles, impacts and future directions, *J. Membr. Sci.* 542 (2017) 378–398.
- [13] S. Zou, Y.-N. Wang, F. Wicaksana, T. Aung, P.C.Y. Wong, A.G. Fane, C.Y. Tang, Direct microscopic observation of forward osmosis membrane fouling by microalgae: critical flux and the role of operational conditions, *J. Membr. Sci.* 436 (2013) 174–185.
- [14] A. Subramani, E.M.V. Hoek, Direct observation of initial microbial deposition onto reverse osmosis and nanofiltration membranes, *J. Membr. Sci.* 319 (2008) 111–125.

- [15] Y. Liu, E. Rosenfield, M. Hu, B. Mi, Direct observation of bacterial deposition on and detachment from nanocomposite membranes embedded with silver nanoparticles, *Water Res.* 47 (2013) 2949–2958.
- [16] A.I. Radu, M.S.H. van Steen, J.S. Vrouwenvelder, M.C.M. van Loosdrecht, C. Picioreanu, Spacer geometry and particle deposition in spiral wound membrane feed channels, *Water Res.* 64 (2014) 160–176.
- [17] P.R. Neal, H. Li, A.G. Fane, D.E. Wiley, The effect of filament orientation on critical flux and particle deposition in spacer-filled channels, *J. Membr. Sci.* 214 (2003) 165–178.
- [18] A. Bogler, A. Kastl, M. Spinnler, T. Sattelmayer, A. Be'er, E. Bar-Zeev, Particle counting and tracking: zooming on deposition and flow paths during initial stages of cake formation in forward osmosis with spacers, *J. Membr. Sci.* (2019) 117619.
- [19] Ultrasensitive detection technology, in: I. Johnson, M.T.Z. Spence (Eds.), *Mol. Probes Handb. A Guid. To Fluoresc. Probes Labeling Technol.*, eleventh ed., 2010.
- [20] S.S. Bucs, R.V. Linares, J.O. Marston, A.I. Radu, J.S. Vrouwenvelder, C. Picioreanu, Experimental and numerical characterization of the water flow in spacer-filled channels of spiral-wound membranes, *Water Res.* 87 (2015) 299–310.
- [21] G. Schock, A. Miquel, Mass transfer and pressure loss in spiral wound modules, *Desalination* 64 (1987) 339–352.
- [22] C. Shankaraman, M.R. Wiesner, Particle transport in clean membrane filters in laminar flow, *Environ. Sci. Technol.* 26 (1992) 1611–1621.
- [23] Y.-L. Li, T.-H. Chang, C.-Y. Wu, C.-J. Chuang, K.-L. Tung, CFD analysis of particle deposition in the spacer-filled membrane module, *J. Water Supply Res. Technol. - Aqua* 55 (2006) 589–601.
- [24] J. Altmann, S. Ripperger, Particle deposition and layer formation at the crossflow microfiltration, *J. Membr. Sci.* 124 (1997) 119–128.
- [25] L. Song, M. Elimelech, Particle deposition onto a permeable surface in laminar flow, *J. Colloid Interface Sci.* 173 (1995) 165–180.
- [26] Y. Wang, F. Wicaksana, C.Y. Tang, A.G. Fane, Direct microscopic observation of forward osmosis membrane fouling, *Environ. Sci. Technol.* 44 (2010) 7102–7109.
- [27] A. Tiraferri, N.Y. Yip, A.P. Straub, S. Romero-Vargas Castrillon, M. Elimelech, A method for the simultaneous determination of transport and structural parameters of forward osmosis membranes, *J. Membr. Sci.* 444 (2013) 523–538.
- [28] A.H. Haidari, S.G.J. Heijman, W.G.J. van der Meer, Effect of spacer configuration on hydraulic conditions using PIV, *Separ. Purif. Technol.* 199 (2018) 9–19.
- [29] Z. Cao, D.E. Wiley, A.G. Fane, CFD simulations of net-type turbulence promoters in a narrow channel, *J. Membr. Sci.* 185 (2001) 157–176.
- [30] S.M.F. Hasani, M. Shakaib, M. Mahmood, CFD modeling of unsteady fluid flow and mass transfer in spacer-filled membrane modules, *Desalin. Water Treat.* 9 (2009) 211–220.
- [31] S.-T. Kang, A. Subramani, E.M.V. Hoek, M.A. Deshusses, M.R. Matsumoto, Direct observation of biofouling in cross-flow microfiltration: mechanisms of deposition and release, *J. Membr. Sci.* 244 (2004) 151–165.
- [32] F. Chaumeil, M. Crapper, DEM simulations of initial deposition of colloidal particles around non-woven membrane spacers, *J. Membr. Sci.* 442 (2013) 254–263.
- [33] A.H. Haidari, S.G.J. Heijman, W.G.J. van der Meer, Visualization of hydraulic conditions inside the feed channel of reverse osmosis: a practical comparison of velocity between empty and spacer-filled channel, *Water Res.* 106 (2016) 232–241.